Angewandte Chemie
Eine Zeitschrift der Gesellschaft Deutscher Chemiker

Supporting Information

Atroposelective Access to 1,3-Oxazepine-Containing Bridged Biaryls via Carbene-Catalyzed Desymmetrization of Imines

X. Yang, L. Wei, Y. Wu, L. Zhou, X. Zhang*, Y. R. Chi**

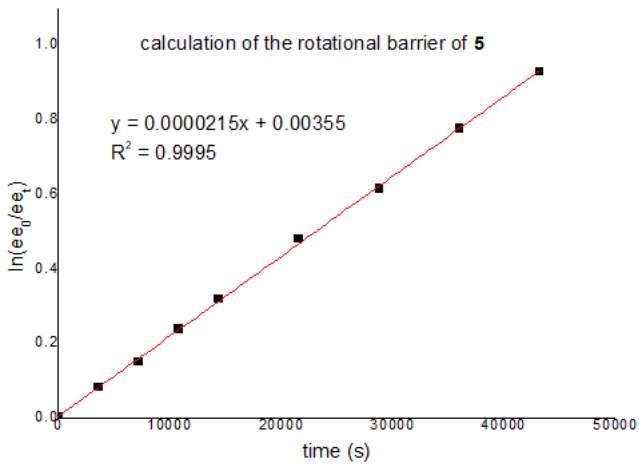

$Ln(ee_0/ee_t) = 2k_{ent}t+C$

k_{ent} = 1/2 slope = 0.0000108 s^{-1}

$k_{rac} = 2k_{ent}$ = 0.0000215 s^{-1}

$t_{1/2rac} = \ln 2/k_{rac}$ = 32239 s = 8.96 h

$\Delta G^{\neq} = -RT\ln(k_{ent}h/k_BT)$ = 28.1 kcal/mol

DFT calculations

Computational Methods

Conformational sampling

Conformational samplings were carried out at GFN2-xTB[4–6] level of theory using the CREST (**C**onformer-**R**otamer **E**nsemble **S**ampling **T**ool) program version 2.12 by Grimme and co-workers.[7,8] The conformers and rotamers ensemble was generated using the iterative metadynamics based on genetic z-matrix crossing (iMTD-GC). Conformers were further optimized at GFN2-xTB level with very tight (*-opt vtight*) optimization in the presence of ALPB implicit solvation model for chloroform (solvent used in the experimental reactions) and for toluene (solvent used in the rotational barriers measurement). The 10 lowest energy conformers were further optimized at density functional theory (DFT) level and the lowest DFT energy comformer is used for further analysis/usage.

Density functional theory (DFT) calculations

DFT calculations were carried out using the *Gaussian 16* rev. B.01 program.[9] The global hybrid functional M06-2X[10] with Karlsruhe-family basis set of double-ζ valence def2-SVP[11,12] for all atoms were employed for all gas-phase optimizations. Single point

(SP) corrections were performed using M06-2X functional and def2-TZVP[11] basis set for all atoms. The implicit SMD continuum solvation model[13] was used to account for the solvent effect of chloroform (solvent used in the experimental reactions) and of toluene (solvent used in the rotational barriers measurement). Gibbs energies were evaluated at the room temperature (for reaction) and at 70ºC (for rotational barriers measurements), using the entropic quasi-harmonic treatment scheme of Grimme[14] and the enthalpy quasi-harmonic treatment of Head-Gordon,[14] at a cut off frequency of 100 cm^{-1}. The free energies were further corrected using standard concentration of 1 mol/L, which was used in solvation calculations. Data analysis was carried out using the GoodVibes code version 3.1.1.[15] Gibbs energies evaluated at SMD(chloroform/ toluene)-M06-2X/def2-TZVP//M06-2X/def2-SVP level of theory are given in kcal/mol. Non-covalent interactions (NCIs) were analyzed using NCIPLOT[16] calculations. The *.wfn* files for NCIPLOT were generated at M06-2X/def2-SVP level of theory. NCI indices calculated with NCIPLOT were visualized at a gradient isosurface value of $s = 0.5$ au. These are colored according to the sign of the second eigenvalue (λ_2) of the Laplacian of the density ($\nabla^2\rho$) over the range of –0.1 (blue = attractive) to +0.1 (red = repulsive). Molecular orbitals are visualized using an isosurface value of 0.05 au throughout. All molecular structures and molecular orbitals were visualized using *PyMOL* software.[17]

Computational rotational barriers studies

The rotational barriers for the enantiomerization of the structures **2a**, **2z**, **2ab** and **5** (Scheme S1) are studied computationally. For structure **5** which has many degrees of freedom, thorough conformational sampling was carried out using the CREST program[7,8] at GFN2-xTB[4–6] level in the presence of ALPB implicit toluene. A relaxed PES scan of the dihedral angle along the C–C axial axis is performed, in accordance to the protocol outlined in reference.[12] The highest energy structure is then used as the guess structure to locate the actual rotational transition structure. The TSs for the enantiomerization via rotation for each of these structures were then successfully located and verified by intrinsic reaction coordinate (IRC)[18,19] analyses (see attached IRC movies, on DOI: 10.5281/zenodo.6789750, for details).

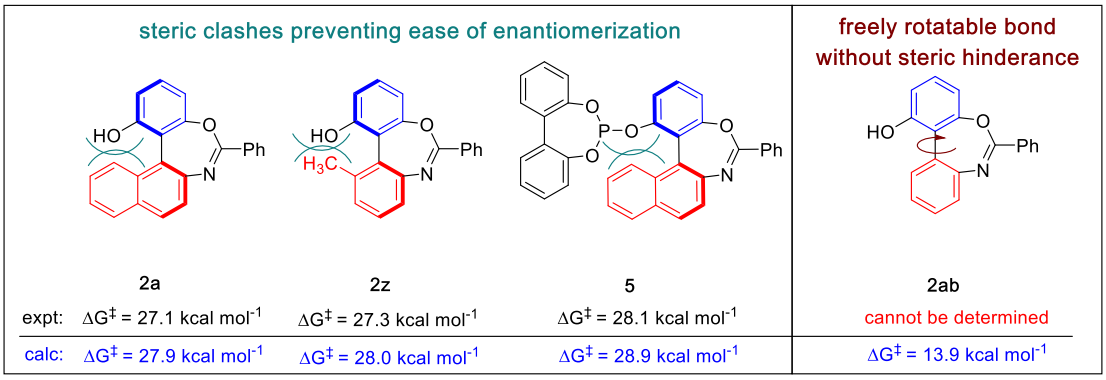

Scheme S1. Structures for which the transition states for their enantiomerization are studied. The experimentally determined rotational barriers are shown.

Figure S1 shows the DFT optimized structures of the transition states of the enantiomerization of these structures. We can see that the DFT-computed rotational barriers are in very good agreement with the experimentally obtained barriers; the computed barriers for structures **2a**, **2z**, and **5** are 27.9 kcal mol^{-1}, 28.0 kcal mol^{-1} and 28.9 kcal mol^{-1}, respectively, which are within 1 kcal mol^{-1} of the experimentally determined barriers (Scheme S1).

Structure	Reactant	TS for enantiomerization
2a	$\Delta G^{\ddagger}$ = 0.0 kcal mol^{-1}	$\Delta G^{\ddagger}$ = 27.9 kcal mol^{-1}
	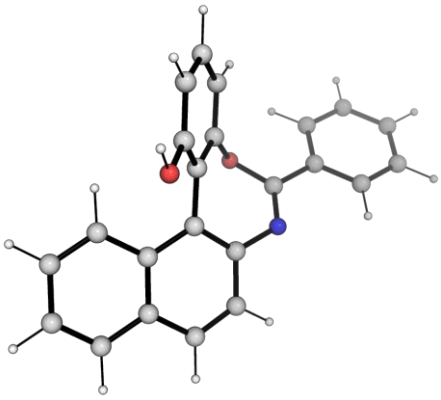	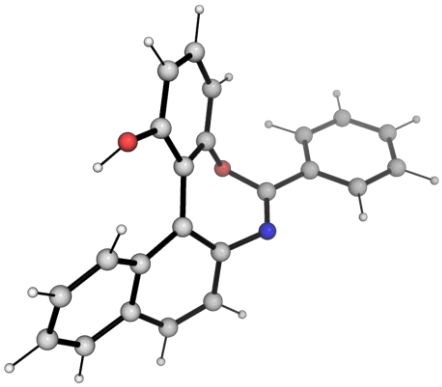
2z	$\Delta G^{\ddagger}$ = 0.0 kcal mol^{-1}	$\Delta G^{\ddagger}$ = 28.0 kcal mol^{-1}

	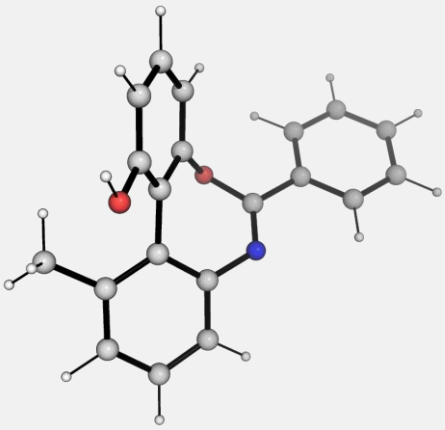	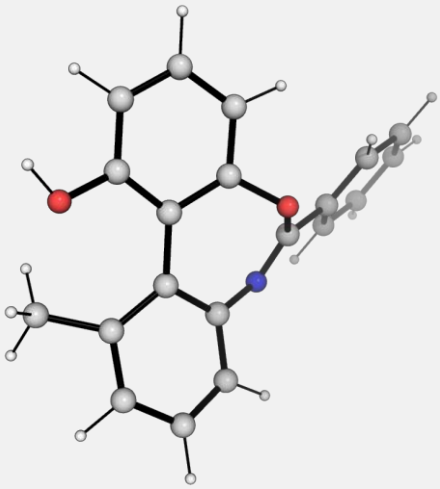
2ab	$\Delta G^{\ddagger}$ = 0.0 kcal mol^{-1}	$\Delta G^{\ddagger}$ = 13.9 kcal mol^{-1}
	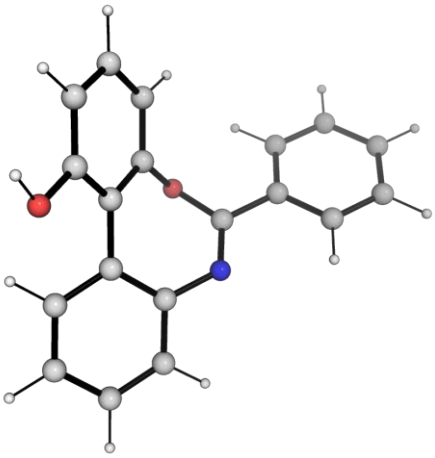	
5	$\Delta G^{\ddagger}$ = 0.0 kcal mol^{-1}	$\Delta G^{\ddagger}$ = 28.9 kcal mol^{-1}
	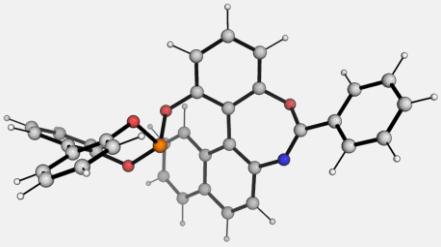	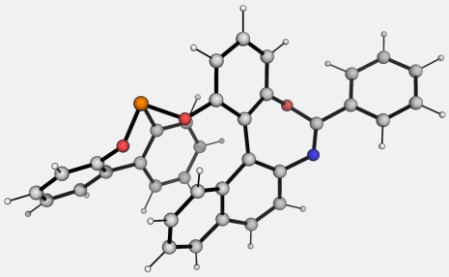

Figure S1. DFT-optimized transition state structures for the enantiomerization of various structures. Computed rotational barriers are taken relative to each structure as the "reactant". Rotational barriers are calculated at SMD(toluene)-M06-2X/def2-TZVP//M06-2X/def2-SVP level of theory at 70ºC and are given in kcal mol^{-1}.

Structure **2ab** is computed to have a rotational barrier of 13.9 kcal mol^{-1}. This translates to a half-life of 1.8 millisecond (*ms*) at room temperature, and for example, 28.5*s* at -60ºC and 15 minutes at -80 ºC using simple transition state theory for estimation. Thus,

structure **2ab** is expected to enantiomerize rapidly and no enantiomeric excess (ee) can be observed at the reaction condition.

From these studies, we see that the *ortho*-substituent on the phenyl ring is essential in preventing easy enantiomerization by offering steric hinderance to rotation along the axis such that distinct enantiomers can exist at the reaction conditions/temperature (structures **2a**, **2z** and **5** in Scheme S1), whereas the lack of the substituent at this position (structure **2ab**) allows for free rotation along the axial axis, making the enantiomerization easy to occur and the product non-resolvable (Scheme S1).

Enantioselectivity determining transition state

To study the origin of the experimentally observed enantioselectivity, we focused on the enantio-determining step, which is the attack of the imine carbon atom in the azolium intermediate by the two different hydroxyl groups (Scheme S2).

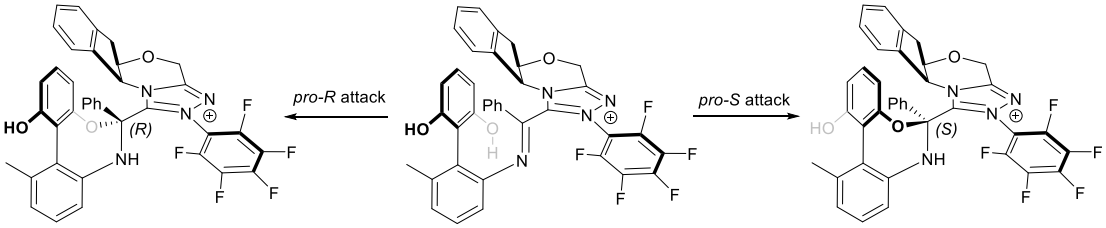

Scheme S2. Schematic representations of the enantio-determining step arising from the attack of the imine carbon by different hydroxyl (–OH) groups.

The lowest energy conformer for the azolium intermediate was found via GFN2-xTB CREST conformational sampling followed by DFT optimization of the 10 lowest energy conformers and taking the lowest energy structure on the DFT potential energy surface (PES). We tried to locate the TSs for these C–O bond formation event, however, to no success. The relaxed PES scan along the bond forming C–O distance suggest that there may not be any TSs for the C–O bond formation for this azolium intermediate, as the PES scan plots in Figure S2 shows that the C–O covalently bonded structures formed via this intermediate would be very thermodynamically uphill (~60–80 kcal mol^{-1}).

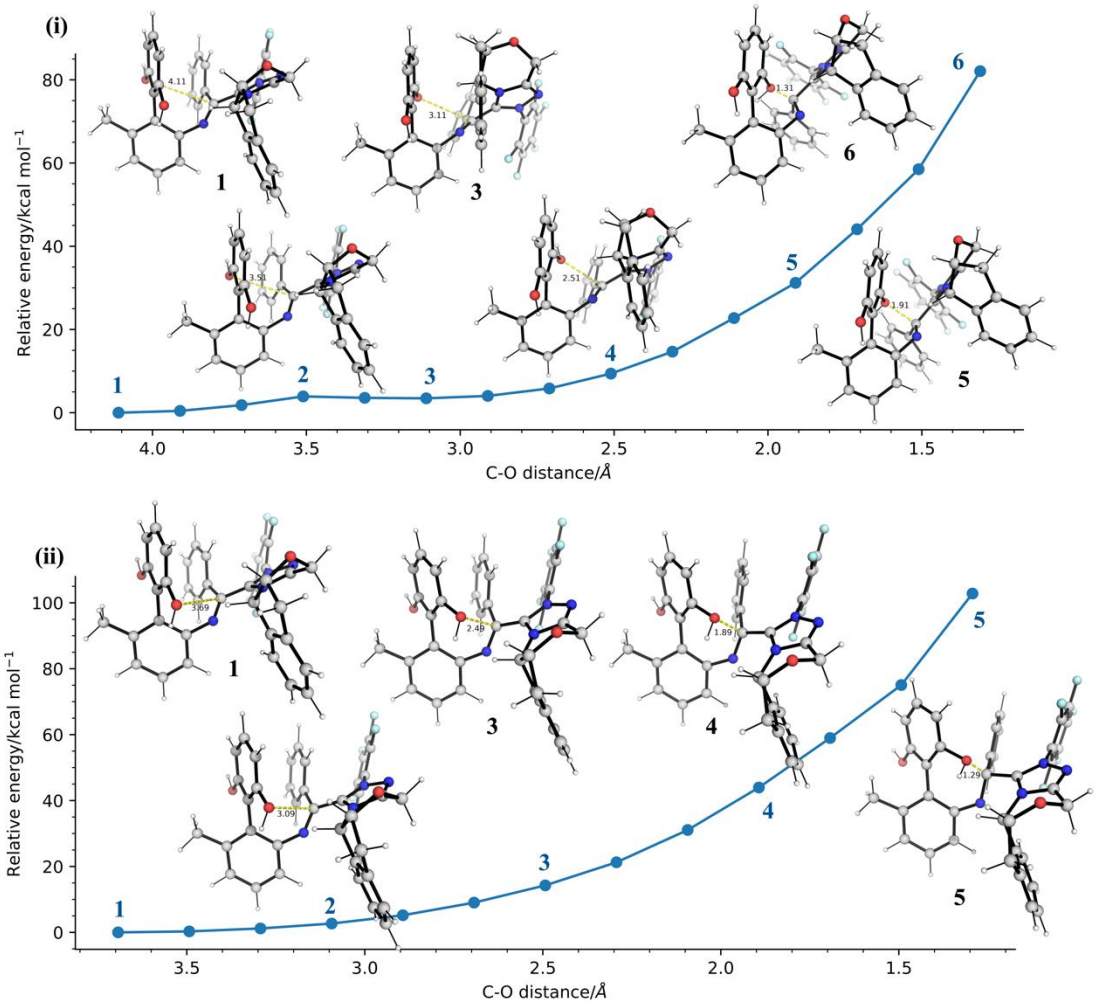

Figure S2. Relaxed potential energy surface (PES) scan for the C–O bond formation for (i) *pro-R* attack and (ii) *pro-S* attack computed at M06-2X/def2-SVP level of theory. Energies are taken relative to the lowest energy conformer from CREST+DFT optimization (structures at point **1**) and their units are given in kcal mol^{-1}. Note that both attacks result from the attack of the *(Si)*-face of the imine.

We hypothesized that the phenol OH groups may be *reversibly* deprotonated by the base present in the reaction and since we are interested in the *relative* barrier difference between the two enantiogenic reaction pathways, we considered instead the TSs for which the deprotonated phenoxide attacks the imine C=N carbon. The TSs for these two pathways leading to different enantiomeric outcomes are shown in Figure S3.

From the frontier molecular orbitals (FMOs) analysis (HOMOs and LUMOs) in Figure S3, we can see that there is productive overlap between the HOMO and the LUMO in **TS-major**, as we can see that in this TS structure, as the C–O σ bond is formed, the

HOMO shows $\sigma_{C–O}$ orbital and the LUMO shows $\sigma^*_{C–O}$ orbital. On the other hand, there is no such productive orbital overlap in **TS-minor**; in fact, the HOMO shows $\sigma^*_{C–O}$ anti-bonding characteristics not favorable for C–O σ bond formation. The non-covalent interaction (NCI) plots show that both TS structures benefit from π-π interactions between the aryl rings, although it is hard to quantify numerically which is more favorable from the NCI plots alone.

	TS-major	**TS-minor**
ΔΔG‡	0.0 kcal mol^{-1}	8.3 kcal mol^{-1}
DFT structure	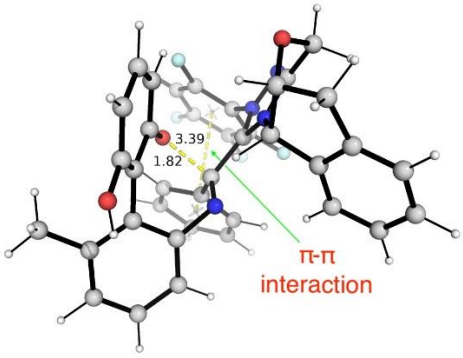	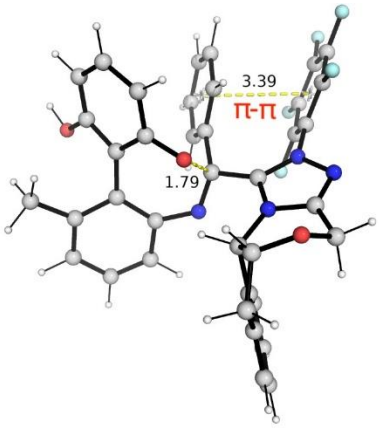
HOMO	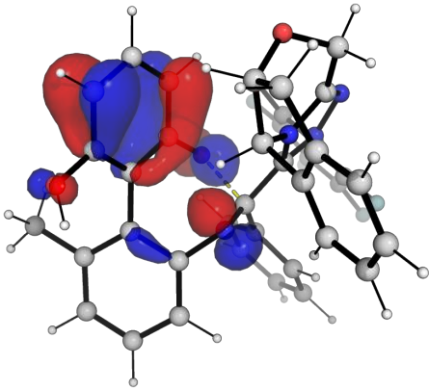	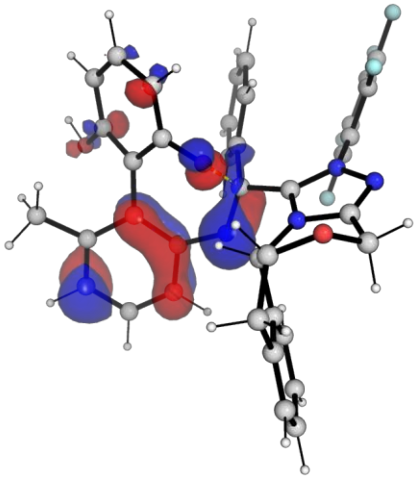

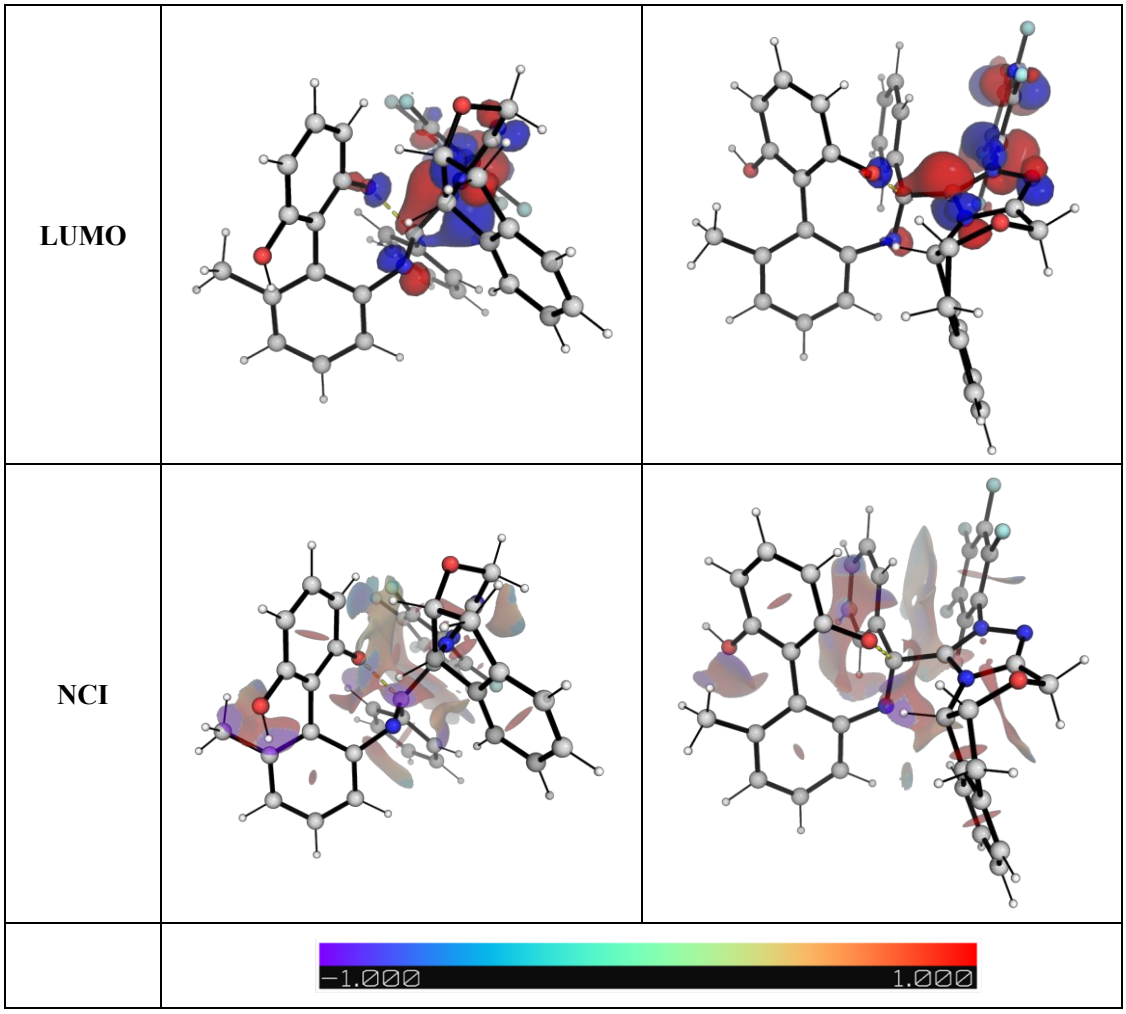

Figure S3. DFT-optimized TS structures, their HOMOs and LUMOs (isosurface value = 0.05 au) and non-covalent interaction (NCI) plots. Key bond distances are given in Å. Relative activation barriers ($\Delta\Delta G^{\ddagger}$) are given in kcal mol^{-1}.

To gain further insights into the origins for the enantioselectivity, we performed a distortion-interaction[20,21]/activation strain (DI-AS) model[21–25] analysis. The DI-AS model is applied to these key TSs. Geometries are taken from along the IRC reaction coordinate at every 3 points interval and single point gas-phase calculations were performed at M06-2x/def2-TZVP level of theory to obtain DI-AS profiles shown in Figure S4. From the plot, we can see that the distortions are similar and indeed the interactions, e.g., arising from productive orbital overlaps, are more favorable in **TS-major**, in agreement with the qualitative FMO analysis outlined above.

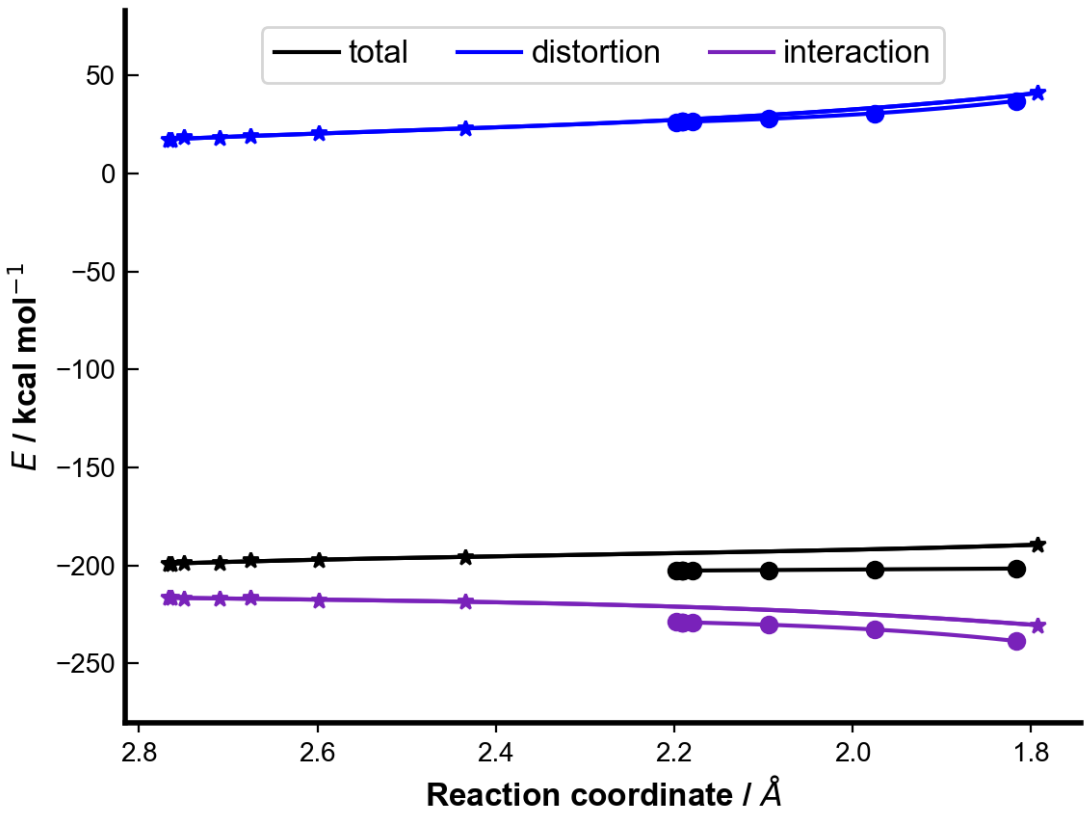

Figure S4. The activation strain or distortion-interaction analyses applied to the IRC paths along the enantio-determining transition states for the major product formation, **TS_major** (in full circle markers) and for the minor product formation, **TS_minor** (in star markers). All energies are calculated at M06-2X/def2TZVPP in gas-phase and used without any further corrections.

Optimized structures and absolute energies, zero-point energies

Geometries of **all optimized structures** (in .xyz format with their associated energy in Hartrees) and **movies of relevant IRC analyses** are included in a separate folder named *DFT_xyz_structures* with an associated readme.txt file. All these data have been uploaded to zenodo.org (DOI: 10.5281/zenodo.6789750).

Absolute values (in Hartrees) for SCF energy, zero-point vibrational energy (ZPE), enthalpy and quasi-harmonic Gibbs free energy for M06-2X/def2-SVP optimized conformers and single point corrections in SMD(chloroform) and SMD(toluene) using M06-2X/def2-TZVP functional are also included.

Reaction in chloroform at room temperature						
Structures	**E/au**	**ZPE/au**	**H/au**	**T.S/au**	**qh-G/au**	**SP SMD(chloroform) M06-2X/def2TZVP**
azolium_intermediate	-2404.632404	0.576779	-2404.0145	0.112084	-2404.124898	-2407.410891
azolium_intermediate_c2	-2404.632404	0.576779	-2404.0145	0.112073	-2404.124893	-2407.410895
azolium_intermediate_c3	-2404.631826	0.576909	-2404.0139	0.110037	-2404.123171	-2407.41172
azolium_intermediate_c4	-2404.627097	0.576836	-2404.0091	0.111341	-2404.119286	-2407.40892
azolium_intermediate_c5	-2404.627097	0.576839	-2404.0091	0.111334	-2404.119279	-2407.408921
azolium_intermediate_c6	-2404.627097	0.576839	-2404.0091	0.111334	-2404.119279	-2407.40892
azolium_intermediate_c7	-2404.627097	0.576839	-2404.0091	0.111334	-2404.119279	-2407.40892
azolium_intermediate_c8	-2404.628587	0.576936	-2404.0105	0.111493	-2404.120662	-2407.407794
azolium_interm	-2404.626571	0.576685	-2404.0088	0.110973	-2404.118611	-2407.407717

ediate_c9						
azolium_intermediate_c10	-2404.630864	0.577324	-2404.0126	0.11033	-2404.121951	-2407.408342
TS_major	-2404.190044	0.564275	-2403.5864	0.106169	-2403.692056	-2406.923720
TS_minor	-2404.168133	0.563523	-2403.5652	0.106584	-2403.670891	-2406.909806

Rotational barriers in toluene at 70ºC temperature

Structures	**E/au**	**ZPE/au**	**H/au**	**T.S/au**	**qh-G/au**	**SP SMD(toluene) M06-2X/def2TZVP**
structure_2z_c1	-975.257279	0.303297	-974.93005	0.075448	-975.00527	-976.351019
structure_2z_c2	-975.252813	0.302787	-974.92591	0.075746	-975.001403	-976.348351
TS_2z	-975.209407	0.302432	-974.88387	0.073406	-974.956819	-976.304921
structure_2ab_c1	-935.992428	0.275517	-935.69495	0.071469	-935.766135	-937.043127
structure_2ab_c2	-935.988846	0.275186	-935.69156	0.071782	-935.763047	-937.040873
TS_2ab	-935.967993	0.27453	-935.67174	0.072578	-935.743107	-937.01781
structure_2a_c1	-1089.462521	0.322975	-1089.1141	0.078707	-1089.192478	-1090.679728
structure_2a_c2	-1089.456658	0.322525	-1089.1085	0.079073	-1089.187254	-1090.675833

TS_2a	-1089.414947	0.322051	-1089.0681	0.077147	-1089.144865	-1090.632020
structure_5	-2042.009443	0.485312	-2041.4835	0.115706	-2041.596027	-2044.043655
structure_5_c2	-2042.009443	0.485311	-2041.4835	0.115704	-2041.596027	-2044.043655
structure_5_c3	-2042.009443	0.485312	-2041.4835	0.115699	-2041.596024	-2044.043656
structure_5_c4	-2042.011153	0.485274	-2041.4853	0.114743	-2041.597321	-2044.044057
structure_5_c5	-2042.011153	0.485274	-2041.4853	0.114743	-2041.597321	-2044.044057
structure_5_c6	-2042.011397	0.485264	-2041.4856	0.11382	-2041.5971	-2044.043975
structure_5_c7	-2042.01202	0.485083	-2041.4863	0.115084	-2041.598361	-2044.042934
structure_5_c8	-2042.012341	0.485234	-2041.4866	0.112541	-2041.597339	-2044.041603
structure_5_c9	-2042.012341	0.485233	-2041.4866	0.11254	-2041.597338	-2044.041602
structure_5_c10	-2042.012341	0.485233	-2041.4866	0.112538	-2041.597339	-2044.041600
TS_5	-2041.972592	0.484544	-2041.4485	0.109402	-2041.556388	-2044.000321

X-ray structure of 2k

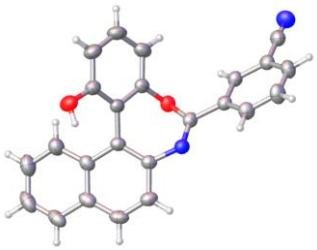

Deposition No. CCDC 2182790

≡

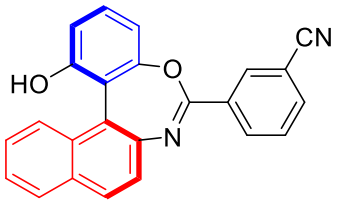

2k

References

[1] a) Yang, G.; Guo, D.; Meng, D.; Wang, J. *Nat. Commun.* **2019**, *10, 3062*; b) Lu, S.; Poh, S. B.; Rong, Z.; Zhao, Y. *Org. Lett.* **2019,** *21*, 6169−6172.

[2] Bai, S.-T.; Kluwer, A. M.; Reek, J. N. H. *Chem. Commun.* **2019**, *55*, 14151−14154.

[3] Ahmed, A.; Bragg, R. A.; Clayden, J.; Lai, L. W.; McCarthy, C.; Pink, J. H.; Westlund, N.; Yasin, S. A. *Tetrahedron* **1998**, *54*, 13277–13294.

Full reference for Gaussian software:

Gaussian 16, Revision B.01, Frisch, M. J.; Trucks, G. W.; Schlegel, H. B.; Scuseria, G. E.; Robb, M. A.; Cheeseman, J. R.; Scalmani, G.; Barone, V.; Mennucci, B.; Petersson, G. A.; Nakatsuji, H.; Caricato, M.; Li, X.; Hratchian, H. P.; Izmaylov, A. F.; Bloino, J.; Zheng, G.; Sonnenberg, J. L.; Hada, M.; Ehara, M.; Toyota, K.; Fukuda, R.; Hasegawa, J.; Ishida, M.; Nakajima, T.; Honda, Y.; Kitao, O.; Nakai, H.; Vreven, T.; Montgomery Jr., J. A.; Peralta, J. E.; Ogliaro, F.; Bearpark, M.; Heyd, J. J.; Brothers, E.; Kudin, K. N.; Staroverov, V. N.; Kobayashi, R.; Normand, J.; Raghavachari, K.; Rendell, A.; Burant, J. C.; Iyengar, S. S.; Tomasi, J.; Cossi, M.; Rega, N.; Millam, J. M.; Klene, M.; Knox, J. E.; Cross, J. B.; Bakken, V.; Adamo, C.; Jaramillo, J.; Gomperts, R.; Stratmann, R. E.; Yazyev, O.; Austin, A. J.; Cammi, R.; Pomelli, C.; Ochterski, J. W.; Martin, R. L.; Morokuma, K.; Zakrzewski, V. G.; Voth, G. A.; Salvador, P.; Dannenberg, J. J.; Dapprich, S.; Daniels, A. D.; Farkas, Ö.; Foresman, J. B.; Ortiz, J. V; Cioslowski, J.; Fox, D. J. Gaussian, Inc., Wallingford CT, **2016**.

(1) Bannwarth, C.; Ehlert, S.; Grimme, S. GFN2-XTB - An Accurate and Broadly Parametrized Self-Consistent Tight-Binding Quantum Chemical Method with Multipole Electrostatics and Density-Dependent Dispersion Contributions. *J.*

Chem. Theory Comput. **2019**, *15* (3), 1652–1671.

(2) Grimme, S.; Bannwarth, C.; Shushkov, P. A Robust and Accurate Tight-Binding Quantum Chemical Method for Structures, Vibrational Frequencies, and Noncovalent Interactions of Large Molecular Systems Parametrized for All Spd-Block Elements (Z = 1-86). *J. Chem. Theory Comput.* **2017**, *13* (5), 1989–2009.

(3) Bannwarth, C.; Caldeweyher, E.; Ehlert, S.; Hansen, A.; Pracht, P.; Seibert, J.; Spicher, S.; Grimme, S. Extended Tight-Binding Quantum Chemistry Methods. *Wiley Interdiscip. Rev. Comput. Mol. Sci.* **2021**, *11* (2).

(4) Grimme, S. Exploration of Chemical Compound, Conformer, and Reaction Space with Meta-Dynamics Simulations Based on Tight-Binding Quantum Chemical Calculations. *J. Chem. Theory Comput.* **2019**, *15* (5), 2847–2862.

(5) Pracht, P.; Bohle, F.; Grimme, S. Automated Exploration of the Low-Energy Chemical Space with Fast Quantum Chemical Methods. *Phys. Chem. Chem. Phys.* **2020**, *22* (14), 7169–7192.

(6) Weigend, F.; Ahlrichs, R. Balanced Basis Sets of Split Valence, Triple Zeta Valence and Quadruple Zeta Valence Quality for H to Rn: Design and Assessment of Accuracy. *Phys. Chem. Chem. Phys.* **2005**, *7* (18), 3297–3305.

(7) Weigend, F. Accurate Coulomb-Fitting Basis Sets for H to Rn. *Phys. Chem. Chem. Phys.* **2006**, *8* (9), 1057–1065.

(8) Li, Y. P.; Gomes, J.; Sharada, S. M.; Bell, A. T.; Head-Gordon, M. Improved Force-Field Parameters for QM/MM Simulations of the Energies of Adsorption for Molecules in Zeolites and a Free Rotor Correction to the Rigid Rotor Harmonic Oscillator Model for Adsorption Enthalpies. *J. Phys. Chem. C* **2015**, *119* (4), 1840–1850.

(9) Luchini, G.; Alegre-Requena, J. V.; Funes-Ardoiz, I.; Paton, R. S.; Pollice, R. GoodVibes: Automated Thermochemistry for Heterogeneous Computational Chemistry Data. **2020**, *9*, 291.

(10) Contreras-García, J.; Johnson, E. R.; Keinan, S.; Chaudret, R.; Piquemal, J. P.; Beratan, D. N.; Yang, W. NCIPLOT: A Program for Plotting Noncovalent Interaction Regions. *J. Chem. Theory Comput.* **2011**, *7* (3), 625–632.

(11) Schrödinger, L. *The PyMOL Molecular Graphics Development Component, Version 1.8*; 2015.

(12) Lv, Y.; Luo, G.; Liu, Q.; Jin, Z.; Zhang, X.; Chi, Y. R. Catalytic Atroposelective Synthesis of Axially Chiral Benzonitriles via Chirality Control during Bond Dissociation and CN Group Formation. *Nat. Commun. 2022 131* **2022**, *13* (1), 1–9.

(13) Fukui, K. The Path of Chemical Reactions - The IRC Approach. *Acc. Chem. Res.* **1981**, *14* (12), 363–368.

(14) Fukui, K. Formulation of the Reaction Coordinate. *J. Phys. Chem.* **2005**, *74* (23), 4161–4163.

(15) Ess, D. H.; Houk, K. N. Distortion/Interaction Energy Control of 1,3-Dipolar Cycloaddition Reactivity. *J. Am. Chem. Soc.* **2007**, *129* (35), 10646–10647.

(16) Bickelhaupt, F. M.; Houk, K. N. Analyzing Reaction Rates with the Distortion/Interaction-Activation Strain Model. *Angew. Chem. Int. Ed.* **2017**, *56* (34), 10070–10086.

(17) Bickelhaupt, F. M. Understanding Reactivity with Kohn-Sham Molecular Orbital Theory: E2-SN2 Mechanistic Spectrum and Other Concepts. *J. Comput. Chem.* **1999**, *20* (1), 114–128.

(18) Fernández, I.; Bickelhaupt, F. M. The Activation Strain Model and Molecular Orbital Theory: Understanding and Designing Chemical Reactions. *Chem. Soc. Rev.* **2014**, *43* (14), 4953–4967.

(19) Wolters, L. P.; Bickelhaupt, F. M. The Activation Strain Model and Molecular Orbital Theory. *Wiley Interdiscip. Rev. Comput. Mol. Sci.* **2015**, *5* (4), 324–343.

(20) Vermeeren, P.; van der Lubbe, S. C. C.; Fonseca Guerra, C.; Bickelhaupt, F. M.; Hamlin, T. A. Understanding Chemical Reactivity Using the Activation Strain Model. *Nat. Protoc.* **2020**, *15* (2), 649–667.